

Ultrathin gradient nonlinear metasurface with a giant nonlinear response

NISHANT NOOKALA,¹ JONGWON LEE,^{1,2} MYKHAILO TYMCHENKO,¹ J. SEBASTIAN GOMEZ-DIAZ,¹ FREDERIC DEMMERLE,³ GERHARD BOEHM,³ KUEIFU LAI,⁴ GENNADY SHVETS,⁴ MARKUS-CHRISTIAN AMANN,³ ANDREA ALU,^{1,*} AND MIKHAIL BELKIN^{1,5}

¹Department of Electrical and Computer Engineering, The University of Texas at Austin, Austin, Texas 78712, USA

²School of Electrical and Computer Engineering, Ulsan National Institute of Science and Technology (UNIST), Ulsan, 44919, South Korea

³Walter Schottky Institut, Technische Universität München, Am Coulombwall 4, Garching 85748, Germany

⁴Department of Physics, The University of Texas at Austin, Austin, Texas 78712, USA

⁵e-mail: mbelkin@ece.utexas.edu

*Corresponding author: alu@ece.utexas.edu

Received 11 January 2016; revised 16 February 2016; accepted 16 February 2016 (Doc. ID 257095); published 8 March 2016

Gradient metasurfaces have recently been demonstrated to provide control of the phase of scattered fields over sub-wavelength scales, enabling a broad range of linear optical components in a flat, ultrathin, integrable platform. Additionally, the development of *nonlinear metasurfaces* has disrupted conventional nonlinear optical device design by relaxing phase matching constraints, reducing size and dimensionality, and providing record values of localized nonlinear responses. However, extending the “flat optics” paradigm to the nonlinear case faces important challenges, since we are required to simultaneously achieve efficient frequency conversion and sub-diffractive phase control. Here, we experimentally demonstrate continuous phase control of the giant nonlinear second harmonic optical response from metasurfaces tied to intersubband transitions in semiconductor multi-quantum wells, establishing an exciting path toward realizing the vision of flat, nonlinear optics. © 2016 Optical Society of America

OCIS codes: (160.3918) Metamaterials; (250.5403) Plasmonics; (190.2620) Harmonic generation and mixing; (190.5970) Semiconductor nonlinear optics including MQW.

<http://dx.doi.org/10.1364/OPTICA.3.000283>

1. INTRODUCTION

Gradient metasurfaces, i.e., ultrathin optical components with engineered transverse impedance gradients along the surface, have recently been demonstrated to provide control of the phase of the scattered fields over subwavelength scales, enabling a broad range of “flat” linear optical components in an ultrathin, integrable platform [1–5]. More recently, optical metamaterials with tailored nonlinear responses have provided new degrees of freedom in metamaterial design, with potential applications such as super-resolution imaging [6], frequency conversion with greatly relaxed phase-matching conditions [7], and in all-optical switching and memories at the nanoscale [8]. It is highly desirable to extend the concept of “flat optics” [5] to the nonlinear case, leading to ultrathin nonlinear optical metasurfaces with embedded features that are able to fully control the wavefront of the nonlinear output. This new paradigm faces important challenges, since it is required to simultaneously achieve *high conversion efficiency* and *sub-diffractive phase control* over ultrathin, deeply subwavelength, and largely uncoupled structures.

To achieve efficient frequency conversion in a nonlinear metasurface of sub-wavelength thickness, the product of the second-order nonlinear response $\chi^{(2)}$ and the pump electric field intensity

E_{pump} must be $|\chi^{(2)}E_{\text{pump}}| \approx 1$ (see Supplement 1). In traditional nonlinear crystals, this condition is achieved when the pump field intensity is comparable with atomic fields (see, e.g., [9, p. 3]), which inevitably leads to material damage. Thus, any practical, flat, nonlinear optical system must have a nonlinear response much higher than that of traditional materials to enable the $|\chi^{(2)}E_{\text{pump}}| \approx 1$ condition for pump intensities below the material’s damage threshold. Nonlinear metasurfaces based on plasmonic nanoresonators demonstrated previously in the infrared/visible frequencies [10–13] have second-order nonlinear elements $\chi^{(2)} \sim 1\text{--}100$ pm/V. Pump intensities ranging from 10 TW/cm² to over 100 PW/cm² are needed to achieve $|\chi^{(2)}E_{\text{pump}}| \approx 1$. Such intensities are only possible with high-power ultrafast lasers and are well above the metal damage threshold. As a result, second harmonic generation (SHG) power conversion efficiencies below 10^{-10} were achieved in these structures using femtosecond pulses with intensities ~ 0.1 GW/cm² [10–13].

Ultrathin metasurfaces based on coupling electromagnetic modes in plasmonic nanoresonators with quantum-engineered intersubband nonlinearities in multi-quantum-well (MQW) semiconductor heterostructures have been shown to exhibit very strong nonlinear responses [14–16]. This approach allows one to

harness and enhance the intrinsically large nonlinear susceptibility of MQW structures, $\chi_{\text{MQW},zzz}^{(2)}$, which is polarized in the direction normal to the surface [17], to engineer ultrathin metasurfaces with giant effective nonlinear susceptibility tensor components in the metasurface plane $\chi_{ijk}^{(2)}$ ($i, j = x$ or y). We have recently reported deeply subwavelength ($\sim\lambda/20$) MQW-based metasurfaces with a record-high second-order nonlinear susceptibility of 10^6 pm/V at $\lambda \approx 10$ μm and experimentally achieved conversion efficiencies up to 0.075% using pumping intensities of only ~ 15 kW/cm² [14–16], well below the material damage threshold even for a continuous-wave operation. Based on a similar concept, conversion efficiencies up to 0.14% for pulse operation and relatively high-power incident beams have been reported in [15]. These nonlinear metasurfaces may provide the foundation for the proposed flat nonlinear optics paradigm if we can find an efficient way to enable the continuous control of the phase of the giant nonlinear response at the individual nanoresonator level.

Toward this goal, we have recently theoretically described a generalization of the Pancharatnam–Berry (PB) phase approach to nonlinear optics [18], which enables controlling the phase of the nonlinear optical response at the individual nanoresonator level by engineering its rotation in the metasurface plane. We note that, in contrast to the formalism presented in [11], our theoretical approach does not impose any restriction on the nanoresonator shape, and it is applicable to any configuration, including the nonsymmetrical nanoresonators used in MQW-based metasurfaces that are able to maximize the nonlinear optical response. Very recently, several approaches have also been introduced to control the phase of the nonlinear (NL) wavefront, including the binary modulation of the resonators [15,19], the adiabatic rotation of symmetrical nanostructures [11], and the modification of the aspect ratio of gold nanocavities [20]. These techniques have then been applied to demonstrate functionalities such as beam steering and focusing of the nonlinear generated beam. Even though these approaches enable full manipulation of the NL phase of the generated beam, they do not necessarily enable a strong nonlinear response, and consequently lead to metasurfaces with small conversion efficiencies that cannot be employed in practice. Here, we report the first experimental demonstration of an MQW-based PB nonlinear gradient metasurface. We *simultaneously* achieve a giant second-order nonlinear optical response of over 3×10^5 pm/V and full 360 deg phase control of the nonlinear optical response at the individual nanoresonator level.

We operate on a circular polarization (CP) basis, transforming the metasurface susceptibility tensor elements from $\chi_{ijk}^{(2)}$ (where i, j , and k can be the x or y of a Cartesian coordinate system with a z -axis normal to the metasurface) into $\chi_{\alpha\beta\gamma}^{(2)}$, where α, β , and γ are R or L , corresponding to right circular polarization (RCP) or left circular polarization (LCP), respectively, of the input (the last two indices) or the output (the first index) beams normal to the surface. It can then be shown (see Supplement 1 and [18]) that, on this circular-polarization basis, the local phase of the generated SH signal in each cell is linearly proportional to the orientation angle φ of its plasmonic resonator. More specifically, assuming the RCP pump beam, a varying rotation angle $\varphi(x)$ of the nanoresonator along the x direction of the metasurface results in a phase factor $\exp[-3i\varphi(x)]$ and $\exp[-i\varphi(x)]$ for the RCP and LCP components of the second harmonic output, respectively. Importantly, the magnitude of the second harmonic (SH) response remains

nearly constant for all nanoresonator rotation angles, as long as the nanoresonator geometry is not changed [9].

These features are ideal for the purpose of locally controlling the phase of the giant nonlinear response in MQW-based metasurfaces. Different from conventional PB approaches based on linear phenomena [21,22], whose overall efficiency is largely dependent on the resonator design, here we can easily split the design of nonlinear gradient metasurfaces into two distinct steps. First, we focus on the design of optimal MQWs and nanoresonators to provide the largest possible localized nonlinear response. Then, we rotate the optimized nanoresonator design in different unit cells to imprint the desired transverse phase pattern onto the metasurface plane.

2. METASURFACE DESIGN

The semiconductor MQW heterostructure design employed in this work and its associated second-order nonlinear optical susceptibility $\chi_{\text{MQW},zzz}^{(2)}$ are shown in Figs. 1(a) and 1(b), respectively. The heterostructure is designed to support giant nonlinear SHG at $1/\lambda \approx 1015$ cm⁻¹ ($\lambda \approx 9.85$ μm or 125 meV photon energy) with a nonlinear response as high as $\sim 2.8 \times 10^5$ pm/V, 3–4 orders of magnitude higher than the largest $\chi^{(2)}$ coefficient of natural optical materials [9,23]. Unlike the doubly resonant MQW designs (with $\omega_{12} = \omega_{23}$) used in MQW-based metasurfaces previously [14,15], the transition energy between states 1 and 2 in the MQW design used in this work is purposely detuned by approximately 25 meV from the pump photon energy to reduce optical losses in the nanoresonator cavity and avoid the saturation of the nonlinear optical responses by the pump light. Saturation in MQWs occurs when the input intensity is so large that the intersubband absorption empties the quantum-well ground state, limiting the maximum achievable overall nonlinear response of the MQW system [14]. The analyses presented in

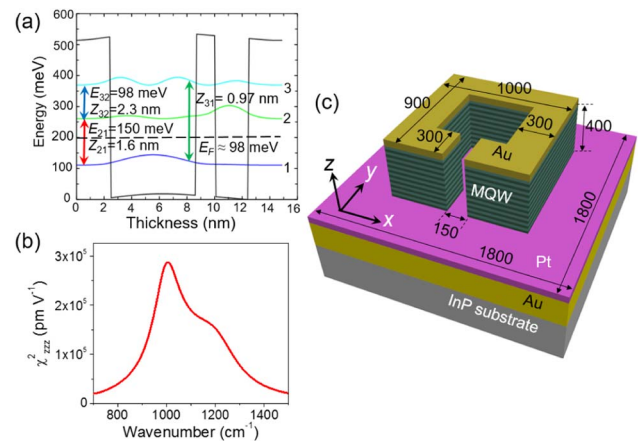


Fig. 1. Nonlinear metasurface structure. (a) Conduction band diagram of one period of an $\text{In}_{0.53}\text{Ga}_{0.47}\text{As}/\text{Al}_{0.48}\text{In}_{0.52}\text{As}$ quantum well structure designed for giant nonlinear SHG response. Shown are the square of the electron subband wavefunctions and the intersubband transition energies and dipole moments. The layer sequence in nm is 2.5/6.2/1.4/2.4/2.5, where $\text{Al}_{0.48}\text{In}_{0.52}\text{As}$ barriers are shown in bold, and the first 1.5 nm of the first 2.5 nm-barrier and the last 1.5 nm of the last 2.5 nm-barrier are n-doped to 6×10^{18} cm⁻³. (b) Second-order nonlinear susceptibility for SHG in MQW structure in (a) as a function of the pump frequency. (c) 1800 nm \times 1800 nm unit cell of the metasurface with the key dimensions given in nm.

[16,24] indicated that the saturation of the MQW nonlinearity is reduced and overall SHG efficiency may be improved by detuning the transition energy between states 1 and 2 away from the pump frequency. Overall, the MQW structure employed here supports a nearly 7 times higher saturation intensity and a 6 times higher $\chi_{MQW,zzz}^{(2)}$ than the MQW structure reported in [14], the latter being achieved by increasing MQW doping.

For the design of the metasurface unit cell, we focused on the split-ring resonator (SRR) depicted in Fig. 1(c), which offers a small spatial footprint in all dimensions, and a square unit cell that allows arbitrary rotation. Details of the fabrication procedure of these structures are given later on. In contrast to the resonators used in previously published MQW-based metasurfaces [14,18], which were made of metal patterning on top of a continuous MQW layer, the resonators used in this work are open metal-semiconductor nanocavities with the MQW layer outside of the nanoantenna pattern etched away. Due to the large contrast between the permittivity of the MQW substrate and the air gap, this approach leads to the significant enhancement of the field intensities at the fundamental and second harmonic frequencies in the MQW layer, and reduction of the cross-talk between adjacent nanoresonators, as confirmed by numerical simulations. The resonator dimensions and unit cell have been optimized to provide strong absorption for x -polarized beams at the fundamental frequency (FF) and for y -polarized beams at the second harmonic frequency for a cell with $\varphi = 0$, i.e., without any rotation. This enables the efficient coupling of x -polarized light at the fundamental frequency to z -polarized intersubband transitions in the MQW and provides efficient outcoupling of the z -polarized nonlinear polarization in the MQW layer to the y -polarized beam at the second harmonic frequency [14]. The computed normalized z -polarized electric field distribution in the MQW structure 100 nm below the top metal surface in the nanoresonators is shown in Fig. 2(a) for the case of excitation with x -polarized fundamental light at $1/\lambda \approx 1015 \text{ cm}^{-1}$ (left panel) and y -polarized second-harmonic light at $1/\lambda \approx 2030 \text{ cm}^{-1}$ (right panel). These wavenumbers correspond to the maximum of the MQW nonlinear response, as shown in Fig. 1(b). The computed fields are normalized to the input (transverse) field amplitude, and the simulations show up to 3 times more local field enhancement in the MQW layer. Figure 2(a) confirms that the proposed structure possesses strong resonances at both frequencies of interest. The overall nonlinear response of the metasurface can be obtained by computing its nonlinear susceptibility tensor using the expression [14]

$$\chi_{ijk}^{(2)} = \chi_{MQW,zzz}^{(2)} \frac{\int_{UC} \xi_i^{2\omega}(x, y, z) \xi_j^{\omega}(x, y, z) \xi_k^{\omega}(x, y, z) dV}{V}, \quad (1)$$

where ξ_i^{ω} ($\xi_i^{2\omega}$) is the local enhancement of the induced z -polarized E-field in the MQW structure normalized to the i -polarized incident wave at ω (2ω), and the expression in the square brackets is the nonlinear overlap integral between the fundamental and second harmonic modes of the nanoantenna with the integration going over the entire unit cell volume (see Supplement 1). Our numerical calculations produce $\chi_{yxx}^{(2)} = 2.4 \times 10^5 \text{ pm/V}$ and $\chi_{yxy}^{(2)} = \chi_{yyx}^{(2)} = 0.4 \times 10^5 \text{ pm/V}$, with the other components of the $\chi^{(2)}$ tensor of the metasurface in the Cartesian coordinate system being much lower. On the CP basis,

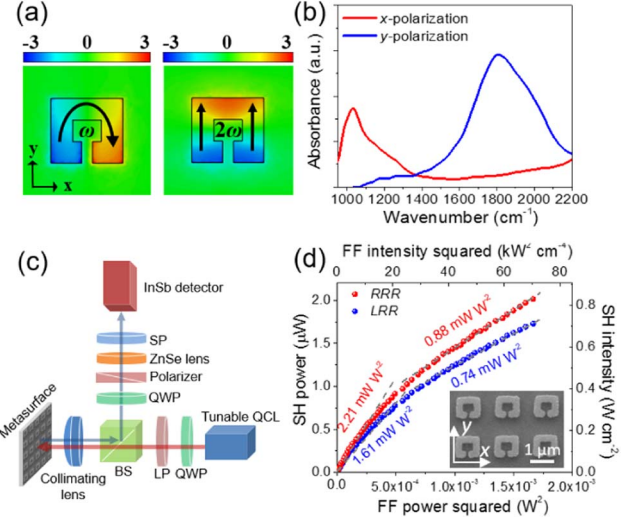


Fig. 2. (a) Simulated normalized E_z field distribution in MQW layer of proposed SRR structures. The SRRs are doubly resonant at the FF and SH. They are seen responding to x -polarized light at the FF, and y -polarized at the SH. (b) Experimental absorption spectrum of fabricated SRR structures, demonstrating resonance at FF and SH as described. (c) Optical setup for second harmonic power characterization. Linearly polarized light from a tunable QCL at wavenumber 1015 cm^{-1} passes through a QWP and is converted to RCP light, followed by long-pass filter to block the SH from the laser, and is focused onto an array of un-rotated SRRs by a numerical aperture 0.5 collimating lens. The generated second harmonic reflects off the beam splitter and is converted to linearly polarized light after passing through another QWP. RCP and LCP SH light is discriminated by the linear polarizer, and the resulting beam is focused onto a liquid-nitrogen cooled InSb detector after passing through an SP to block out FF reflection from the pump. (d) SH peak power (left axis) or peak intensity (right axis) as a function of the FF peak power squared (bottom axis) or peak intensity squared (top axis). Inset: Scanning electron microscope (SEM) image of fabricated SRR structure.

the second-order nonlinear susceptibility tensor elements are $\chi_{RRR}^{(2)} = \chi_{LLL}^{(2)} = 1.1 \times 10^5 \text{ pm/V}$ and $\chi_{LRR}^{(2)} = \chi_{RLL}^{(2)} = 0.6 \times 10^5 \text{ pm/V}$.

3. CHARACTERIZATION

To perform the initial characterization of our metasurface design, we fabricated a $300 \mu\text{m} \times 300 \mu\text{m}$ metasurface made of the unit cells shown in Fig. 1(c) with the same orientation of SRRs in all cells. A 390 nm-thick MQW layer composed of 26 repetitions of the MQW structure depicted in Fig. 1(a) was grown via molecular beam epitaxy on a semi-insulating InP substrate. The growth started with a 300 nm-thick etch-stop layer of $\text{In}_{0.53}\text{Ga}_{0.47}\text{As}$, followed by a 100 nm-thick etch-stop layer of InP, and finished with the MQW layer. A 10 nm-thick layer of titanium, a 50 nm-thick layer of platinum, and a 200 nm-thick layer of gold were sequentially evaporated on top of the MQW layer. The wafer was then thermo-compressively bonded epi-side down to another semi-insulating InP wafer coated with the same metal layers. The epi-side substrate of the resulting sandwiched wafer was then removed by mechanical polishing and selective chemical wet etching, followed by the removal of the etch-stop layers via selective wet etching to expose the MQW layer. A 5 nm-thick layer of titanium and a 50 nm-thick layer of gold were evaporated on top of the exposed MQW layer, followed by plasma-enhanced chemical vapor

deposition of a 250 nm-thick silicon nitride hard-mask layer. The nanoresonators with the dimensions depicted in Fig. 1(c) were then patterned on the silicon nitride layer via electron beam lithography, and the patterns were etched through the silicon nitride and MQW layers via inductively coupled plasma reactive ion plasma etching, and finally finished by the removal of the silicon nitride mask layer.

The resulting metasurface exhibited the linear absorption characteristics shown in Fig. 2(b), with strong resonances at $1/\lambda \approx 1050 \text{ cm}^{-1}$ for x -polarized excitation and $1/\lambda \approx 1850 \text{ cm}^{-1}$ y -polarized SH resonance. The experimentally measured resonance positions were close to the target values of $1/\lambda \approx 1015 \text{ cm}^{-1}$ and $1/\lambda \approx 2030 \text{ cm}^{-1}$, corresponding to the target fundamental and SHG frequencies. For the characterization we used the setup shown in Fig. 2(c), where we employed a pulsed broadly tunable quantum cascade laser (QCL) tuned to 1015 cm^{-1} as the input pump source. The laser was modulated at 250 kHz, with 400 ns pulses (duty cycle 10%). Linearly polarized light from the QCL passes through a quarter-wave plate (QWP) to convert into circular polarization, then through a long-pass filter to filter out the SH signal from the QCL, a nonpolarizing achromatic 50/50 beam splitter (BS) angled at 45 deg, and a collimating lens with a focal spot diameter of 35 μm to the sample. The SHG beam from the metasurface traces the incident FF beam path backward to the beam splitter and is reflected toward the InSb detector, passing through a QWP designed for the second harmonic frequency and a linear polarizer to filter out the LCP or RCP components of the SH beam. The beam is then focused by a ZnSe lens onto a calibrated InSb detector. A short-pass filter (SP) in front of the InSb detector filters out any FF component in the reflected beam. The fundamental power was measured at the sample position, and the SHG power output was corrected for the beam splitter reflectivity (53.5%) and the transmission of the collimating lens (95%), the quarter-wave plate (95%), the polarizer (75%), the ZnSe lens (97%), and the short-pass filter (91.7%) in the setup.

The SHG peak power (left axis) as a function of the pump peak power squared (bottom axis) and the pump peak intensity squared (top axis) for the SRR metasurface with no rotation is plotted in Fig. 2(d) for RCP FF input, RCP SH output (RRR) and RCP FF input, LCP SH output (LRR) polarization combinations, from which effective nonlinear susceptibilities of $|\chi_{RRR}^{(2)\text{eff}}| = 4.2 \times 10^5 \text{ pm/V}$ ($3.1 \times 10^5 \text{ pm/V}$) and $|\chi_{LRR}^{(2)\text{eff}}| = 3.6 \times 10^5 \text{ pm/V}$ ($2.9 \times 10^5 \text{ pm/V}$) for low (high) pump intensity are obtained, with the dependence on intensity due to the intensity saturation in the MQW [14,24]. The values of the nonlinear susceptibility elements are nearly 10 times higher than those reported in [14], and approximately three orders of magnitude higher than those of traditional nonlinear crystals [9,23] and the nonlinear metasurfaces based on plasmonic resonators that are used in the infrared/visible spectrum exhibit values in the range of 1–300 pm/V [9–12]. Further, these values exceed the intrinsic $\chi_{MQW,zzz}^{(2)}$ of the MQW layer, demonstrating the role that the FF and SH modal overlap plays in the design of optimal nanoresonators.

4. GRADIENT NONLINEAR METASURFACE

When the resonators are spatially arranged as shown in Fig. 3, with an angular rotation step of $\Delta\varphi$ between resonators of adjacent unit cells along one direction, the metasurface provides a nonlinear response with a linear phase gradient along the same direction. Then, from basic reflectarray theory [1–5,18], it is easy

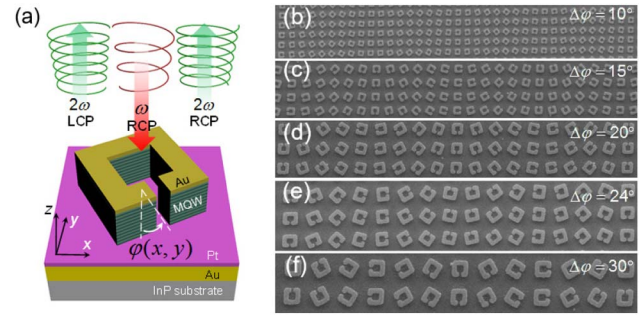


Fig. 3. Phase gradient nonlinear metasurface. (a) Schematic of metasurface unit cell, with cartoon depiction of RCP incident FF light converting to RCP and LCP SH beams. (b)–(f) SEMs of fabricated gradient SRR arrays, with differing angular rotational steps. Five samples with angular steps $\Delta\varphi$ of 10, 15, 20, 24, and 30 deg were fabricated and tested.

to show that a normally incident RCP beam generates two SH beams: one that is RCP polarized toward the direction $\theta_{R(R)} = \arcsin[(3\Delta\varphi/360^\circ)\lambda_{2\omega}/d]$, and another one that is LCP polarized toward $\theta_{L(R)} = \arcsin[(\Delta\varphi/360^\circ)\lambda_{2\omega}/d]$, where $\lambda_{2\omega}$ is the SH wavelength, and d is the width of one unit cell.

To demonstrate SH beam steering, we fabricated metasurfaces with $\Delta\varphi$ of 10, 15, 20, 24, and 30 deg following the same procedure outlined for the nonrotated sample. Scanning electron microscope images of the fabricated linear phase-gradient nonlinear metasurfaces are shown in Figs. 3(b)–3(f). Following the previous formulation, under RCP incidence, we expect to observe RCP (LCP) SH output at 13.3, 20.2, 27.4, 33.5, and 43.7 (4.4, 6.6, 8.8, 10.6, and 13.3) deg for $\Delta\varphi$ of 10, 15, 20, 24, and 30 deg, respectively.

For the far-field measurements, we used a continuous-wave CO₂ laser operating at 9.83 μm to illuminate our PB metasurface samples. The beam was directed through a QWP to convert it into RCP light, chopped at 400 Hz (duty cycle of 50%), and focused onto our sample by a ZnSe lens [$f = 6 \text{ in.}$ (15.24 cm), beam spot diameter of 100 μm]. The average power at the sample position was measured with a thermopile detector to be approximately 500 mW. Additionally, the QWP was measured to have a retardation of 0.25 λ at a wavelength of 8 μm , and approximately 0.21 λ at the operating wavelength of 9.83 μm . We observed that this imperfect retardation introduces both RCP and LCP components into the incident pump, distorting the CP light into elliptical polarization, and further caused spurious SH signals to be generated at both positive and negative angles with respect to the normal. Therefore, to achieve proper, single-direction beam steering, we had to verify that our FF pump was purely RCP. We accomplished this by noting that the optical path length for either s - and p -polarizations incident on the QWP changes with the introduction of tilt along the fast or slow axis of the QWP, thereby affecting the overall retardation offered by the element. By tilting the QWP by approximately 5 deg along the fast axis, we were able to significantly reduce the ellipticity of the incident FF pump from 1.5 to 1.1, where the ellipticity is defined as the ratio of power along the major to the minor axes of the elliptical beam (for purely RCP or LCP light, the ellipticity is 1).

Slightly different optical setups were used to measure the far field of the SHG output for angles greater and smaller than

~ 15 deg, due to the constraints imposed by the size of our optical components and the numerical aperture of our focusing lens. For angles greater than 15 deg, the setup depicted in Fig. 4(a) was used. Generated SH light from the metasurface passes through an SP to remove any reflected FF light, and the RCP/LCP light is then discriminated via a combination of a QWP and linear polarizer, and is finally incident on a liquid-nitrogen cooled InSb detector. For angles smaller than 15 deg [setup depicted in Fig. 4(b)], we employed a beam splitter angled at 45 deg in front of the chopper to reflect the collimated SHG signal onto the same polarization control optics and InSb detector as in the large angle setup. Angular resolution in this configuration was achieved by noting that SHG away from the surface normal to the sample produces a lateral shift of the SH beam at the detector position. The shift is given as $f \tan \theta$, where f is the focal length of the lens [6 in. (15.24 cm)] and θ is the angle of SHG generation with respect to normal. Thus, by scanning the detector in the direction transverse to the beam path, one can resolve the far-field profile of SHG emission for small angles. The measured results, shown in Fig. 4(c) for the RRR polarization combination and Fig. 4(d)

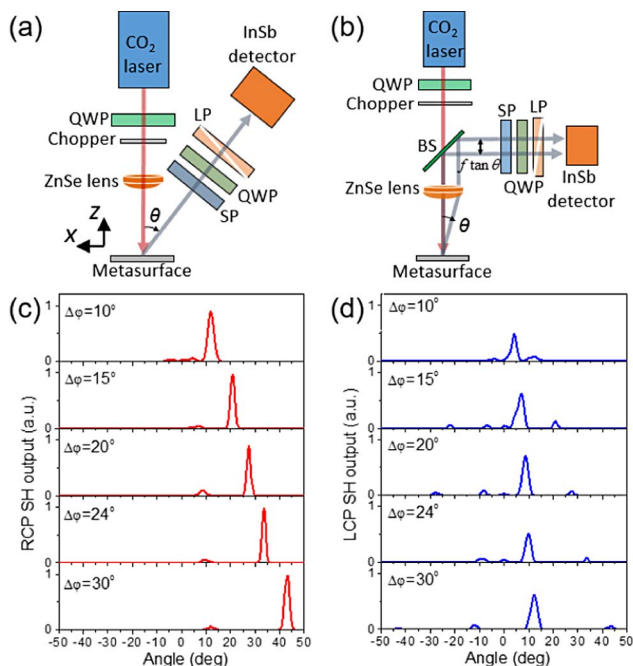


Fig. 4. Phase-gradient nonlinear metasurface characterization. (a) Optical setup for large angle nonlinear beam steering measurement. Linearly polarized light from a continuous-wave CO₂ laser at 1015 cm⁻¹ passes through a QWP to convert to RCP light, followed by a mechanical chopper, and then a ZnSe lens with a 6 in. (15.24 cm) focal length to focus on the sample. The SH beam is generated toward an angle θ , and passes through an SP to remove FF light and through a QWP/linear polarizer to select the LCP or RCP components. The signal is finally detected by an InSb photodetector with approximately 900 $\mu\text{m} \times 900 \mu\text{m}$ sensor size positioned 30 cm away from the sample. (b) Optical setup for small angle NL beam steering measurement. The setup is largely the same as in (a), save for the inclusion of a beam splitter to reflect collimated SH light to the polarization control optics and InSb detector. The angular resolution is determined via detection in the plane transverse to the beam's direction. (c) Far field profiles of RCP SH output from phase-gradient metasurfaces with $\Delta\phi$ of 10, 15, 20, 24, and 30 deg. (d) Same as (c), but for LCP SH output.

for LRR, are in excellent agreement with our predictions, fully confirming the accurate phase control of the generated SH beam with subwavelength resolution. Small peaks appearing in our measurements are explained by the fact that the QWP that we used in the experiment in fact does not provide perfect circular polarization at 1015 cm⁻¹. As a result, for example, the incident “RCP wave” is not purely right-circularly polarized, meaning there is also an LCP pump component, for which the same metasurface steers the SH radiation in other directions. The same effect applies to the analyzer system in the detection setup; that is, when the analyzer is set to transmit only right-circularly polarized SHG light, there is a small LCP SHG component that can reach the detector.

5. CONCLUSION

In summary, we have experimentally demonstrated the generalization of the gradient linear metasurface paradigm introduced in [5] to the nonlinear domain, and theoretically envisioned in [18], by merging optical metasurfaces with giant nonlinear optical responses and the generalized Pancharatnam–Berry phase approach. Our results indicate that we can achieve full control over the phase of the giant nonlinear signal at the individual nanoresonator level. This allows one to attain continuous SHG beam steering, as well as arbitrary patterning of the SHG output wavefront with subwavelength resolution. Future improvements of this approach, both at the MQW and resonator design levels, will lead to highly efficient nonlinear metasurfaces [16,24] that are able to manipulate the generated wavefront at will, unveiling a practical and exciting approach to flat, nonlinear optics.

Funding. Air Force Office of Scientific Research (AFOSR) (FA9550-14-1-0105); Office of Naval Research (ONR) (N00014-10-1-0942); Nano Initiative Munich.

Acknowledgment. The authors would like to acknowledge the help of Dr. Yanan Wang in Prof. Jiming Bao's group at the University of Houston with facilitating the e-beam processing of an earlier generation of samples.

See Supplement 1 for supporting content.

REFERENCES

- N. Yu, P. Genevet, M. A. Kats, F. Aieta, J.-P. Tetienne, F. Capasso, and Z. Gaburro, “Light propagation with phase discontinuities: generalized laws of reflection and refraction,” *Science* **334**, 333–337 (2011).
- X. Ni, N. K. Emani, A. V. Kildishev, A. Boltasseva, and V. M. Shalaev, “Broadband light bending with plasmonic nanoantennas,” *Science* **335**, 427 (2012).
- F. Monticone, N. M. Estakhri, and A. Alù, “Full control of nanoscale optical transmission with a composite metascreen,” *Phys. Rev. Lett.* **110**, 203903 (2013).
- C. Pfeiffer and A. Grbic, “Metamaterial Huygens' surfaces: Tailoring wave fronts with reflectionless sheets,” *Phys. Rev. Lett.* **110**, 197401 (2013).
- N. Yu and F. Capasso, “Flat optics with designer metasurfaces,” *Nat. Mater.* **13**, 139–150 (2014).
- J. B. Pendry, “Time reversal and negative refraction,” *Science* **322**, 71–73 (2008).
- A. Rose and D. R. Smith, “Overcoming phase mismatch in nonlinear metamaterials [Invited],” *Opt. Mater. Express* **1**, 1232–1243 (2011).

8. C. Argyropoulos, P. Y. Chen, F. Monticone, G. D'Aguanno, and A. Alù, "Nonlinear plasmonic cloaks to realize giant all-optical scattering switching," *Phys. Rev. Lett.* **108**, 263905 (2012).
9. R. W. Boyd, *Nonlinear Optics* (Academic, 2008).
10. N. Segal, S. Keren-Zur, N. Hendler, and T. Ellenbogen, "Controlling light with metamaterial-based nonlinear photonic crystals," *Nat. Photonics* **9**, 180–184 (2015).
11. G. Li, S. Chen, N. Pholchai, B. Reineke, P. W. H. Wong, E. Y. B. Pun, K. W. Cheah, T. Zentgraf, and S. Zhang, "Continuous control of the nonlinearity phase for harmonic generations," *Nat. Mater.* **14**, 607–612 (2015).
12. F. B. P. Niesler, N. Feth, S. Linden, J. Niegemann, J. Gieseler, K. Busch, and M. Wegener, "Second-harmonic generation from split-ring resonators on a GaAs substrate," *Opt. Lett.* **34**, 1997–1999 (2009).
13. W. Fan, S. Zhang, K. J. Malloy, S. R. J. Brueck, N. C. Panoiu, and R. M. Osgood, "Second harmonic generation from patterned GaAs inside a subwavelength metallic hole array," *Opt. Express* **14**, 9570–9575 (2006).
14. J. Lee, M. Tymchenko, C. Argyropoulos, P.-Y. Chen, F. Lu, F. Demmerle, G. Boehm, M.-C. Amann, A. Alù, and M. A. Belkin, "Giant nonlinear response from plasmonic metasurfaces coupled to intersubband transitions," *Nature* **511**, 65–69 (2014).
15. O. Wolf, S. Campione, A. Benz, A. P. Ravikumar, S. Liu, T. S. Luk, E. A. Kadlec, E. A. Shaner, J. F. Klem, M. B. Sinclair, and I. Brener, "Phased-array sources based on nonlinear metamaterial nanocavities," *Nat. Commun.* **6**, 7667 (2015).
16. J. Lee, N. Nookala, J. S. Gomez-Diaz, M. Tymchenko, F. Demmerle, G. Boehm, M. Amann, A. Alu, and M. A. Belkin, "Ultrathin second-harmonic metasurfaces with record-high nonlinear optical response," *Adv. Opt. Mater.* (2016).
17. A. E. Rosencher, A. Fiore, B. Vinter, V. Berger, P. Bois, and J. Nagle, "Quantum optical engineering of nonlinearities," *Science* **271**, 168–173 (1996).
18. M. Tymchenko, J. S. Gomez-Diaz, J. Lee, N. Nookala, M. A. Belkin, and A. Alù, "Gradient nonlinear Pancharatnam-Berry metasurfaces," *Phys. Rev. Lett.* **115**, 207403 (2015).
19. E. Almeida, G. Shalem, and Y. Prior, "Nonlinear phase control and anomalous phase matching in plasmonic metasurfaces," <http://arxiv.org/abs/1505.05618>.
20. S. Keren-Zur, O. Avayu, L. Michaeli, and T. Ellenbogen, "Nonlinear beam shaping with plasmonic metasurfaces," *ACS Photon.* **3**, 117–123 (2015).
21. M. V. Berry, "The adiabatic phase and Pancharatnam's phase for polarized light," *J. Mod. Opt.* **34**, 1401–1407 (1987).
22. Z. Bomzon, G. Biener, V. Kleiner, and E. Hasman, "Space-variant Pancharatnam-Berry phase optical elements with computer-generated subwavelength gratings," *Opt. Lett.* **27**, 1141–1143 (2002).
23. Y. R. Shen, *The Principles of Nonlinear Optics* (Wiley-Interscience, 2002).
24. J. S. Gomez-Diaz, M. Tymchenko, J. Lee, M. A. Belkin, and A. Alù, "Nonlinear Processes in multi-quantum-well plasmonic metasurfaces: electromagnetic response, saturation effects, limits and potentials," *Phys. Rev. B* **92**, 125429 (2015).